

Boundary geometry controls topological defect transitions that determine lumen nucleation in embryonic development

Pamela C. Guruciaga,^{1,2,*} Takafumi Ichikawa,^{3,4} Takashi Hiiragi,^{3,4,5,†} and Anna Erzberger^{1,6,‡}

¹*Cell Biology and Biophysics Unit, European Molecular Biology*

Laboratory (EMBL), Meyerhofstraße 1, 69117 Heidelberg, Germany

²*Developmental Biology Unit, European Molecular Biology Laboratory (EMBL), Meyerhofstraße 1, 69117 Heidelberg, Germany*

³*Institute for the Advanced Study of Human Biology (WPI-ASHBi), Kyoto University, Kyoto, 606-8501, Japan*

⁴*Department of Developmental Biology, Graduate School of Medicine, Kyoto University, Kyoto, 606-8501, Japan*

⁵*Hubrecht Institute, Uppsalalaan 8, 3584 CT Utrecht, The Netherlands*

⁶*Department of Physics and Astronomy, Heidelberg University, 69120 Heidelberg, Germany*

(Dated: March 14, 2024)

Topological defects determine the collective properties of anisotropic materials. How their configurations are controlled is not well understood however, especially in 3D, where bulk–surface coupling can render the geometry of confining boundaries relevant. This is particularly important in living matter, where 2D topological defects have been linked to essential biological functions, whereas the role of 3D defects is unclear. Motivated by multicellular systems interacting with extracellular boundaries, we consider a polar fluid confined within curved boundaries imposing weak surface anchoring. We report a novel charge-preserving transition between different defect configurations, controlled by the boundary shape, and invariant to changes in the material parameters. We test if this geometry-driven transition occurs in confined multicellular systems and investigate the biological role of 3D polar defects in the mouse epiblast—an embryonic tissue consisting of apico-basally polarized cells. We find that fluid-filled lumina—structures essential for subsequent embryonic development—tend to form near defect positions of polar fluids in embryo-like confinement geometries. Moreover, by experimentally perturbing embryo shape beyond the transition point, we trigger the formation of additional lumen nucleation sites at the predicted position. Thus, our work reveals how boundary geometry controls polar defects, and how embryos use this mechanism for shape-dependent lumen formation. Because this defect control principle is independent of specific material properties, we expect it to apply universally to systems with orientational order.

* pamela.guruciaga@embl.de

† t.hiiragi@hubrecht.eu

‡ erzberge@embl.de

Confinement plays a fundamental role in directing self-organization [1] in various contexts including colloids [2], developing tissues [3, 4], liquid crystals [5], and crowds of people [6]. Controlling confining structures and predicting their impact on the collective properties of the confined bulk will reveal organisational principles of complex systems such as living matter [7], as well as enable technological applications like the design of optoelectronic [8] and microfluidic [9] devices. Boundary effects permit manipulating the properties of a confined system, which is especially relevant for materials comprised of anisotropic particles, which possess orientational degrees of freedom and tend to align with their neighbours, resulting in long-range order. In liquid crystals, for example, substrates with particular surface topography or chemical functionality [10] favour a uniform parallel or perpendicular orientation of adjacent molecules. This leads to the formation of an ordered layer near the boundary, which propagates into the bulk by elastic forces. In this way, surface-induced alignment [11–13] allows to achieve different desired configurations of the nematic order parameter (OP) via tuning of the boundary conditions. However, the effects of boundary geometry on the bulk organisation of anisotropic materials is not well understood, particularly for curved surfaces in three dimensions.

Confinement also affects how living materials organise internally to carry out biological functions, for example how multicellular systems undergo morphogenesis in biofilms [14] or during embryonic development [15]. The boundary interactions between anisotropic living matter such as tissues which consist of polarised cells, and extracellular matrix (ECM) involve diverse biophysical processes, including adhesion and polarity signaling [16–18], which affect ordering at the collective scale similar to boundary-induced alignment. Basement membrane layers, for example, mechanically and biochemically promote specific orientations of adjacent cells for different types of polarity—parallel for epithelial planar [19, 20] and mesenchymal/migratory polarity [21–23], and perpendicular for apico-basal epithelial polarity [24]. The establishment of coherent apico-basal alignment is a requirement for epithelial functions such as the transport of molecules across the tissue, and is linked to the formation of fluid-filled cavities (lumina) [24]. Orientational boundary effects could give rise to general mechanisms by which confining structures control multicellular organisation.

Many collective properties of ordered materials depend on the number and spatial distribution of topological defects, i.e. points in the OP field where the orientation is not defined. In the case of nematic systems confined to a surface, geometric constraints have been shown to play an important role in determining defect configurations and dynamics [25, 26]. In biological contexts, defects can guide diverse cellular processes [27] and have been shown to trigger the formation of structures such as fruiting bodies [28] and tentacles [29]. However, despite their potential biological role, 3D polar defects and their relation to system geometry have not yet been explored, with most investigations focusing on 2D domains and nematic systems, applicable in multicellular contexts where cells can be approximated as elongated units. These approaches have successfully predicted the collective dynamics of bacterial colonies [28, 30, 31], cell populations [25, 32], and epithelial sheets [33, 34]. However, in many contexts where cellular polarity implies distinct sub-cellular regions with specific functions—for example, in mesenchymal collective cell migration [35, 36]—, the polar nature of cells is relevant for understanding collective structures and properties.

Here, we investigate how the boundary effects of anisotropic media give rise to a surface–bulk coupling that permits controlling the properties of such materials through the geometry of the boundaries. Specifically, we analyse how the mechanical properties and geometry of the boundaries drive the ordering of a 3D polar fluid, and we identify two

transitions in which defects in the OP field appear out of a uniform field, or change their configuration. Moreover, we study the role of boundary geometry on the bulk organization of polarised cells, using the mouse epiblast—the tissue that forms the embryo proper during development—as an example. Orientational order of apico-basal polarity in the epiblast is linked to the formation of a central lumen, a critical event in normal mouse development [37, 38]. By associating the polar OP field with the local average cellular apico-basal polarity in the tissue, we find that 3D-field defect configurations are parameter-free predictors of lumen initiation sites. Moreover, taking advantage of a recently developed *ex vivo* culturing approach [37], we induce additional lumen nucleation sites at the predicted position by experimentally perturbing the shape of the epiblast boundary.

WEAK BOUNDARY-INDUCED ALIGNMENT IN A 3D POLAR FLUID

A polar fluid in a 3D space Ω with total volume V_0 can be characterised by a 3D vector OP $\mathbf{p}(\mathbf{r})$. This local quantity represents the average polarity of individual particles in a volume element [39], and defines the global degree of order

$$P \equiv \langle |\mathbf{p}| \rangle_{\Omega} = \frac{1}{V_0} \int_{\Omega} dV |\mathbf{p}|. \quad (1)$$

The free energy functional of such system is given by

$$\mathcal{F}[\mathbf{p}] = \int_{\Omega} dV f_{\text{B}}(\mathbf{p}, \nabla \mathbf{p}) + \int_{\partial\Omega} dS f_{\text{S}}(\mathbf{p}), \quad (2)$$

where f_{B} and f_{S} are the bulk and surface energy densities, respectively. We minimise equation (2) with respect to variations of the OP and impose boundary conditions

$$\frac{\partial f_{\text{S}}}{\partial p_i} + \hat{\mathbf{n}} \cdot \frac{\partial f_{\text{B}}}{\partial (\nabla p_i)} = 0 \quad \text{in } \partial\Omega, \quad (3)$$

where $\hat{\mathbf{n}}$ is the outward-facing normal, to obtain the Euler–Lagrange equations for the three components p_i (see [Supplementary information](#))

$$\frac{\partial f_{\text{B}}}{\partial p_i} - \nabla \cdot \frac{\partial f_{\text{B}}}{\partial (\nabla p_i)} = 0 \quad \text{in } \Omega. \quad (4)$$

Note that equations (3) ensure continuity of the OP on the boundary, coupling it to its value in the bulk.

Based on the Landau–de Gennes approach to the nematic–isotropic transition in liquid crystals [40], we write the bulk energy density as the sum of thermotropic and elastic contributions, $f_{\text{B}} = f_{\text{T}} + f_{\text{E}}$. To focus on order induced by boundary effects, we consider a regime in the isotropic phase close to the phase transition to the spontaneously ordered state, keeping terms up to second order in the OP: $f_{\text{T}} = a|\mathbf{p}|^2/2$ with $a \gtrsim 0$. The elastic term is given by the Frank free energy density

$$f_{\text{E}} = \frac{k}{2} \left\{ (\nabla \cdot \mathbf{p})^2 + [\mathbf{p} \cdot (\nabla \times \mathbf{p})]^2 + [\mathbf{p} \times (\nabla \times \mathbf{p})]^2 \right\} \quad (5)$$

taken in the one-constant approximation, in which splay, twist, and bend distortions [respectively, the three terms in equation (5)] are penalised with the same coefficient $k > 0$ [41]. These parameters define the correlation length of the material $\xi \equiv \sqrt{k/a}$.

The surface energy density $f_S = f_A + \gamma$ contains the uniform surface tension γ and an interaction energy f_A between the fluid and the confining surface $\partial\Omega$. We consider a weak anchoring interaction [42–46], where the value of the OP at the boundary is not fixed as in the strong case [11–13, 47]. Deviations from the *preferred value* at the surface, \mathbf{p}_0 , are penalised according to the anchoring strength $w > 0$ [44, 45, 48] as

$$f_A = \frac{w}{2} (\mathbf{p} - \mathbf{p}_0)^2. \quad (6)$$

The extrapolation length $\zeta \equiv k/w$ characterizes the competition between the surface anchoring and the bulk elastic energy [49]. For convenience, we also define the anchoring length $\lambda \equiv w/a = \xi^2/\zeta$.

REGIMES OF GLOBAL ORDER AND TOPOLOGICAL CHARGE

Surface anchoring is known to control the structure of defects in liquid crystals in the nematic phase [5, 47, 50]. In spherical confinement, a homeotropic boundary condition gives rise to a radial defect in the centre, while a tangential alignment of the nematic director favours the appearance of two surface defects—known as boojums—at the poles. For a polar OP, several tangential orientations are possible, and mixed boundary conditions—with both tangential and normal \mathbf{p}_0 —have not been studied before, although a related problem was considered for a liquid crystal in Ref. [47]. Numerical minimisation of equation (2) (see [Methods](#)) shows different defect structures depending on the preferred orientation in spherical confinement (Figs. 1a and 1b). Whereas the purely normal \mathbf{p}_0 gives rise to a radial defect in the centre as in a nematic system, the field configurations obtained for pole-to-pole and poles-to-equator tangential \mathbf{p}_0 are similar to the flow lines of a passive fluid in contact with an active surface [51] and present one or two toroidal vortex tubes centered on the symmetry axis. The combination of tangential and normal preferred orientations produces a configuration with a hyperbolic point defect on the symmetry axis and a disclination ring around it.

Such mixed boundary conditions are relevant whenever a polar material is in contact with multiple surfaces with different properties. The mouse epiblast, for example, is confined by two distinct interfaces at embryonic day 5: an approximately hemispherical ECM layer, which promotes perpendicular alignment of epiblast apico-basal polarity via biochemical and mechanical processes [37, 52], and a less curved tissue–tissue interface with the extra-embryonic ectoderm, to which cells orient predominantly in parallel (Figs. 1c and 1d). Although the epiblast shape is quite variable, the volume of the tissue at this stage is typically conserved [$\bar{V}_0^{\text{exp}} \approx (2.3 \pm 0.4) \times 10^5 \mu\text{m}^3$, see [Methods](#)].

Motivated by the shape of the mouse epiblast, we systematically examine the role of boundary geometry on 3D polar OP field configurations in the family of axis-symmetric *acorn* shapes, whose geometry is fully parameterized by the ratio $\nu \equiv z_\alpha/R_\beta$ with z_α the height of the spherical-shell cap and R_β the radius of the hemispherical base (see Fig. 1e and [Methods](#)). While $\nu = 0$ corresponds to a flat tissue–tissue interface, values $0 < \nu \leq 1$ (respectively $-1 < \nu < 0$) represent convex (respectively concave) interfaces, with $\nu = 1$ the spherical case. The total volume V_0 is fixed and defines a length scale $R_0 \equiv (3V_0/4\pi)^{1/3}$. For a given boundary geometry, we minimise the free energy functional \mathcal{F} [equation (2)] and evaluate it at the resulting OP field \mathbf{p} to obtain the free energy F . Considering how F depends on ν reveals the preferred shape of the system (Fig. 2a), which arises from the competition between bulk distortion, surface tension, and anchoring. The existence of the latter is a necessary but insufficient condition for the

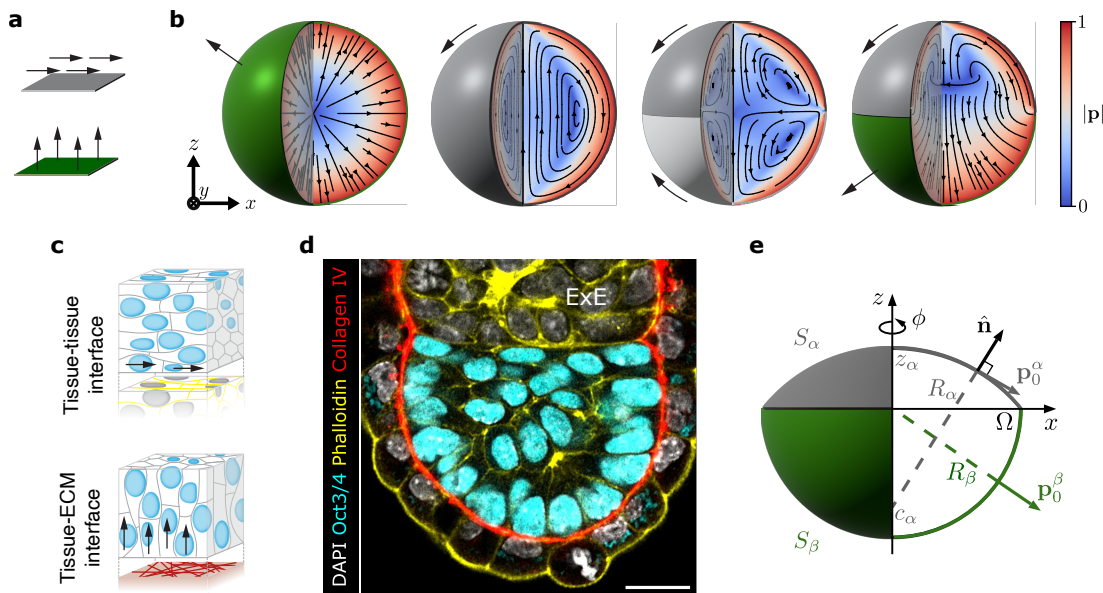


FIG. 1. **Alignment-inducing boundaries with different preferred orientations affect the bulk organisation of a polar material.** **a**, We consider two types of surfaces that favour parallel (gray) or perpendicular (green) preferred orientations \mathbf{p}_0 in a contacting polar fluid. **b**, Streamlines and colour map show the local direction and magnitude of the equilibrium OP field for $\xi/R_0 = 1$ and $\lambda/R_0 = 100$ in a spherical system with varying \mathbf{p}_0 (external arrows). **c**, Apico-basally polarised cells tend to align parallel to a tissue–tissue interface (top) and perpendicular to a tissue–ECM interface (bottom), similar to an anchoring effect [equation (6)]. **d**, Immunofluorescence image shows the central cross-section of a representative mouse embryo after *ex vivo* culture for 18 hours from embryonic day 4.5, stained for an ECM component (Collagen IV), actin (Phalloidin), an epiblast marker (Oct3/4), and DNA (DAPI). At this stage, the epiblast consists of apico-basally polarised cells (cyan nuclei) in contact with a cup-shaped ECM layer (red) and a tissue–tissue interface with the extra-embryonic ectoderm (ExE). Scale bar 20 μm . Adapted from Ref. [37]. **e**, We parameterize the epiblast-like class of acorn shapes with $\nu \equiv z_\alpha/R_\beta$. The base S_β is defined as a hemisphere with radius R_β centred at the origin of coordinates, while the spherical cap S_α has radius R_α , centre $(0, c_\alpha)$ on the symmetry axis, and height z_α . Vectors \mathbf{p}_0^α and \mathbf{p}_0^β depict the mixed preferred orientation on the boundary.

development of global order, as the correlation length must be high enough ($\xi > \xi^* \approx 0.4R_0$) to allow the surface-induced order to penetrate into the bulk (Fig. 2b). For the family of acorn shapes, obtaining the free-energy minima as a function of ν shows that the transition from spherical to flatter shapes—necessary to achieve high values of P —is discontinuous (Figs. 2c and 2d). The location of this transition is modulated by the constant surface tension, which penalizes shapes with large surface-to-volume ratios (Extended Data Fig. 1). Moreover, topological defects appear when $\zeta < \zeta^* \approx 0.3R_0$, comparable to the transition between defect-free and defect-containing states in nematic tactoids [43]. In this regime, boundary anchoring dominates over the bulk, trading off the cost of bulk distortions in favour of better alignment with the preferred orientations at the boundaries (Fig. 2a).

BOUNDARY SHAPE CONTROLS CHARGE-PRESERVING DEFECT TRANSITIONS

To disentangle the role of material parameters and geometry in determining the field structure, we fix the boundary shape and consider changes in the extrapolation length ζ for a constant correlation length. Consistent with our

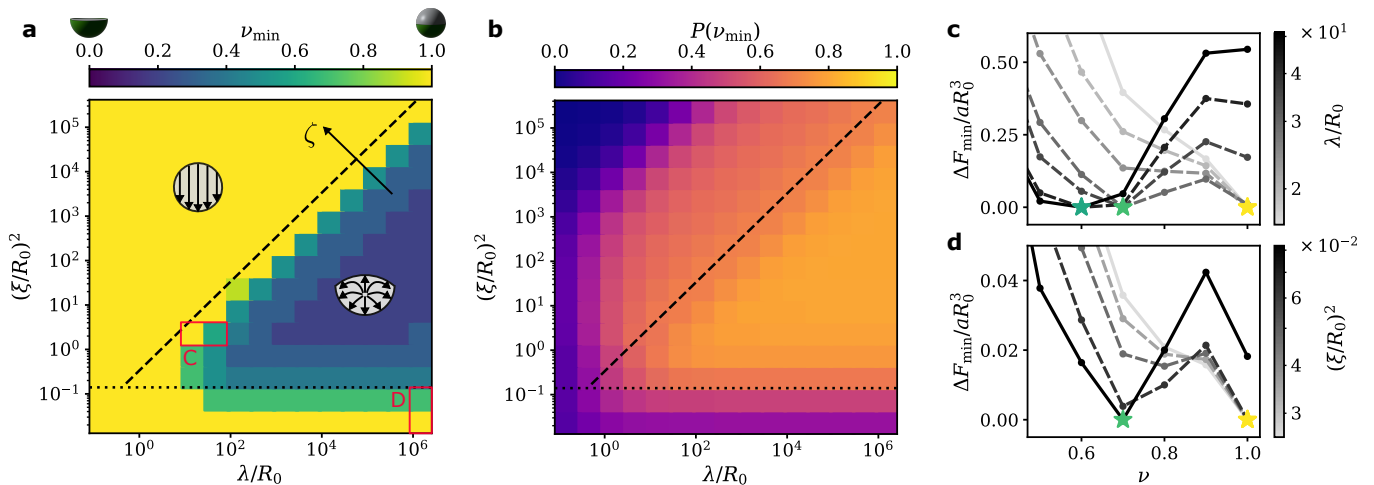


FIG. 2. **Competition between distortion and anchoring determines preferred boundary shape, degree of order, and bulk topological charge.** **a**, Minimizing the free energy F with respect to the shape parameter ν for different values of the correlation length ξ and anchoring length λ yields spherical preferred shapes ν_{\min} with defect-free configurations where bulk elasticity dominates over surface anchoring, and acorns with defects for stronger anchoring. The arrow shows increasing ζ , and insets present typical field configurations for the two regions separated by $\zeta^* \approx 0.3R_0$ (dashed line): with ($\zeta < \zeta^*$) and without ($\zeta > \zeta^*$) defects in the least-energy configurations ($\gamma/aR_0 = 0.2$). **b**, The global degree of order P [equation (1)] of the lowest-energy configuration shows that for $\xi < \zeta^* \approx 0.4R_0$ (dotted line), the system remains disordered (i.e., $P < 0.5$) even in the limit $\lambda \rightarrow \infty$. **c-d**, Energy profiles as functions of the acorn parameter show the appearance and disappearance of minima at the transitions [$\Delta F_{\min} = F - F(\nu_{\min})$]. Continuous lines correspond to the parameter sets marked C (respectively D) in panel **a**, while dashed lines indicate intermediate values. Stars with the same colour code as in panel **a** highlight the position of the global minimum ν_{\min} for the different curves.

previous result, surface-induced alignment dominates for $\zeta < \zeta^*$ and creates defects out of fields that are topologically equivalent to the uniform configuration (Fig. 3a). The number and structure of these defects however depend on the geometry: while for $\nu = 0$ only a pair of radial and positive hyperbolic (hyp-1) hedgehogs are nucleated, a pair of hyp+1 and negative hyperbolic (hyp-1) hedgehogs plus a disclination ring are created for $\nu = 1$. The defect positions change with increasing anchoring length and increasing global order (Fig. 3b). The topological charge for both geometries changes from neutral to +1 when the hyp-1 hedgehog moves up and becomes a hyperbolic boojum on the cap surface [53, 54]. Note that the disclination ring carries no charge and can be collapsed with the hyp+1 hedgehog to render a radial configuration [55].

Given this difference in the defect structure between hemispherical and spherical boundary shapes, we further investigate the impact of geometry by fixing the material length scales in the surface-dominated regime, and varying the acorn shape parameter ν continuously (Figs. 4a and 4b). We find that the defect configuration undergoes a transition from radial hedgehog to a combination of hyp+1 defect plus disclination ring at a critical magnitude of the shape parameter $|\nu| = \nu_c$. Notably, the surface-to-volume ratio and the global degree of order P (Fig. 4c) differ distinctly between the transition points at $-\nu_c$ and ν_c . Measuring the position of the defects (Fig. 4b) shows that their height grows approximately linearly with the acorn parameter, and that the ring is nucleated with a finite radius. This renders the transitions discontinuous, comparable to the first-order transition studied in Ref. [56] in

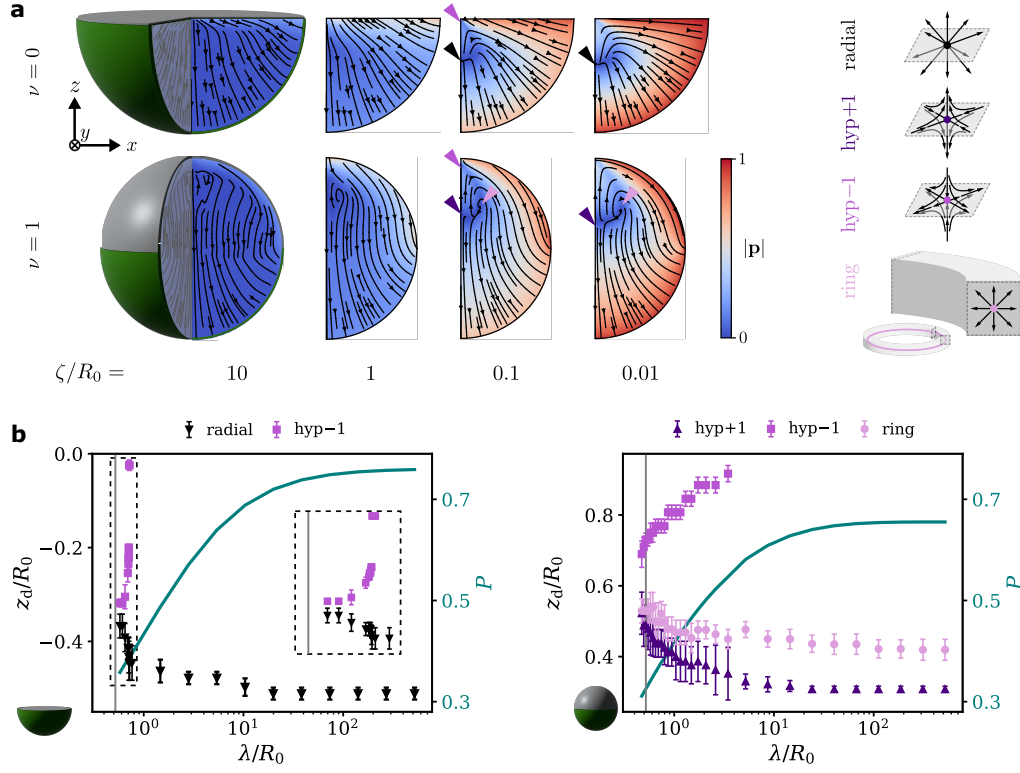


FIG. 3. **Material parameters determine the creation of 3D polar defects.** **a**, The OP fields for decreasing extrapolation length ζ show that groups of defects (coloured arrowheads) are created in order to accommodate the increasingly relevant boundary conditions ($\xi/R_0 = 0.72$). The types of defects differ between hemispherical ($\nu = 0$) and spherical ($\nu = 1$) geometries. Schematics on the right show the configuration of the radial (black), hyp+1 (purple) and hyp-1 (magenta) hedgehogs, and that of the disclination ring (pink). **b**, Increasing the anchoring length λ (equivalent to decreasing ζ) changes the defect height z_d . The hyp-1 bulk defect moves up and becomes a hyperbolic boojum on the surface, while the position of the remaining defects and the global degree of order P reach a plateau as $\lambda \rightarrow \infty$. Points and error bars correspond to the mean and standard deviation of the position of the defect candidates (see [Methods](#)). The vertical line marks the value $\lambda = \xi^2/R_0$ where the anchoring energy overcomes the elastic tendency to a uniform field.

a nematic system with strong homeotropic boundary conditions. Simulations over intervals $\lambda/R_0 \in [10^2, 10^6]$ and $\xi/R_0 \in [\xi^*, \sqrt{\lambda \zeta^*})/R_0$ reveal that the transition point and the position of the defects is robust to changes in material properties (Fig. 4b and Extended Data Fig. 2): the transition from the radial hedgehog to the hyp+1 and ring defects occurs independently of the material parameters at $|\nu_c| = 0.37 \pm 0.03$, and the ring radius changes only 2-fold over an almost three orders of magnitude variation in ξ . In summary, we report a geometry-controlled transition in the defect structure of a 3D confined polar fluid, and show that also the defect locations are robust to changes in the material length scales.

POLAR DEFECTS DETERMINE SITES OF LUMEN NUCLEATION

Topological defects are known to affect large-scale properties of the systems they inhabit [27]. In living systems, 2D nematic defects have been shown to act as organizing centers for biological processes like cell extrusion [33] or

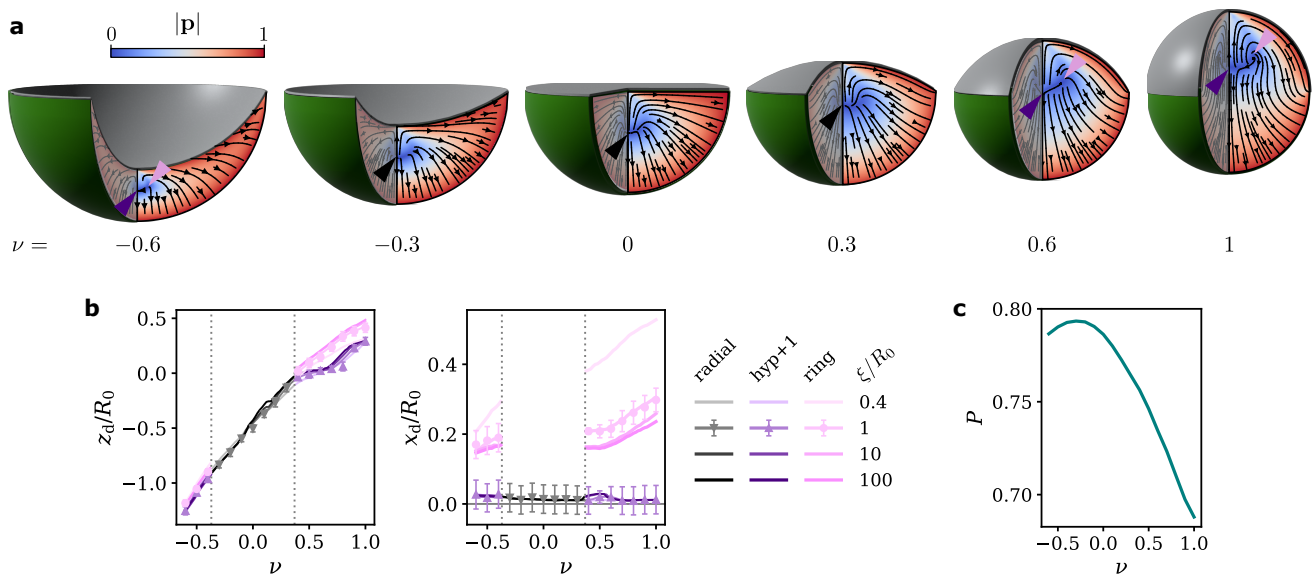


FIG. 4. **Confining geometry controls charge-preserving transitions between different defect configurations.** **a**, The OP fields for representative shapes ν at fixed material length scales $\xi/R_0 = 1$ and $\lambda/R_0 = 10^6$ (i.e., in the highly ordered, defect-containing regime) show transitions between a radial hedgehog (black arrowheads), and a hyp+1 defect (purple arrowheads) surrounded by a disclination ring (pink arrowheads). **b**, The transitions occur when the magnitude of the shape parameter exceeds a critical value $|\nu_c|$ (dotted lines). The transition point is invariant to changes in the material parameters, and defect positions undergo little variation (see also Extended Data Fig. 2). Points and error bars correspond to the mean and standard deviation of the position of the defect candidates (see Methods). **c**, The global degree of order also depends on ν , but the system remains always in the highly ordered ($P > 0.5$) regime.

out-of-plane bending during morphogenesis [57], but how 3D polar defects affect multicellular organisation has not yet been examined. To address this question, we consider the mouse epiblast, and associate the OP \mathbf{p} with the average orientation of apico-basally polarized cells within this confined tissue. We find that small fluid-filled cavities tend to form between the cells near positions where the OP field of a correspondingly confined polar system has radial hedgehog defects (Fig. 5a). Indeed, such lumina typically form between the apical surfaces of cells, which feature distinct molecular compositions and functional properties, with vesicle trafficking or active osmolyte pumps localising asymmetrically along the apico-basal axis [58–61], and 3D polar defects mark positions where contacts between multiple apical surfaces are likely. Importantly, the geometry-driven transition we identified then suggests that tissue shape could control the distribution of lumen nucleation sites, implying that externally manipulating boundary geometry could permit inducing additional lumina. We expect in particular a difference in the spatial distribution and number of lumen nucleation sites between epiblasts with shapes in and out of the range $\nu \in (-\nu_c, \nu_c)$. Specifically, we expect the former to contain sites only close to the central symmetry axis, and the latter to present an additional distribution at a distance similar to the radius of the disclination ring.

To test these predictions, we performed 3D-gel embedded embryo culture (see Ref. [37] and Methods), a technique that faithfully recapitulates *in utero* embryonic development, while allowing for *in toto* monitoring, measurement, and manipulation. Moreover, we experimentally perturbed the shape of the epiblast, specifically the tissue–tissue interface.

The curvature of this interface depends on a preceding morphogenetic event, the inward-folding of the adjacent extra-embryonic ectoderm [37, 62]. Disrupting this process results in embryos with deformed interfaces between the epiblast and this extra-embryonic tissue. We obtained mouse embryos cultured for 18 hours from embryonic day 4.5, of which epiblasts presented various shapes resulting from natural variability in the control condition (Fig. 5a) or experimental manipulation (Fig. 5b) by blocking the formation of the extra-embryonic ectoderm (see Methods). To more accurately account for the shape variations of these embryos, we consider a two-parameter family of shapes, where the base is not a hemisphere but a spherical cap with a center displaced along the symmetry axis (Figs. 5a and 5b, Methods). In addition to ν as previously defined, we introduce a new parameter σ corresponding to the angle between the symmetry axis and the radius from the centre of the base to the point where the two surfaces meet; note that $\sigma_0 = \pi/2$ renders the original acorn family. We fitted this shape model (see Methods) to the boundary segmentation of the central cross-sections of the 16 embryos, obtaining $\nu_{\text{exp}} \in [-0.16, 0.003]$ and $\sigma_{\text{exp}} \in [0.68, 1.43]$ for control embryos ($N = 6$, Fig. 5a), and $\nu_{\text{exp}} \in [0.69, 1.23]$ and $\sigma_{\text{exp}} \in [1.59, 2.41]$ for embryos with a morphogenetic perturbation ($N = 10$, Fig. 5b). We excluded from this analysis embryos which did not undergo elongation of the whole embryo along the distal-proximal axis or did not reach the epiblast cell number of 50 [37]. We also discarded one embryo in which the epiblast–ECM interface was concave and hence incompatible with our family of shapes. We estimated the positions of lumen initiation sites using immunostaining against apical surface components and identified single sites near the central axis in embryos with $|\nu| < \nu_c$, and additional sites as predicted for the majority of embryos with $|\nu| > \nu_c$ (Fig. 5c). Importantly, the defect positions in the OP field for the average shape of control and manipulated embryos predict the average nucleation sites in each group quantitatively (Figs. 5d and 5e). Taken together, these results show that lumina nucleate near polar defect positions, and that the external manipulation of embryo shape permits inducing additional nucleation sites near the position predicted by the geometry-driven defect transition we identified.

DISCUSSION AND OUTLOOK

Confinement and boundary effects can strongly affect the bulk organisation of complex materials. Here, we show how the interaction with confining surfaces drives the creation of different topological defects in the bulk of a polar fluid. We find that the effect of confining geometry is distinct from the role of bulk- and surface-mechanical parameters. While the competition between bulk distortion and surface anchoring governs the transition between defect-free and defect-containing states, the *types* of defects observed and the transitions between different defect configurations depend on the confining geometry alone. Moreover, within the globally ordered regime, the three-dimensional positions of defects prove robust against variation of the Frank constant and the anchoring strength. We thus report a novel charge-preserving defect transition controlled by the geometry of confining surfaces.

In living systems, topological defects impact large-scale spatial organisation not only via distortion effects but also because defect points often trigger local responses through the localization of regulatory molecules that drive subsequent biological processes [27]. Examples include the activation of cell–death signals leading to localized cell extrusion [33], or the assembly of organisational centers during morphogenesis [57, 63]. For the mouse epiblast—a

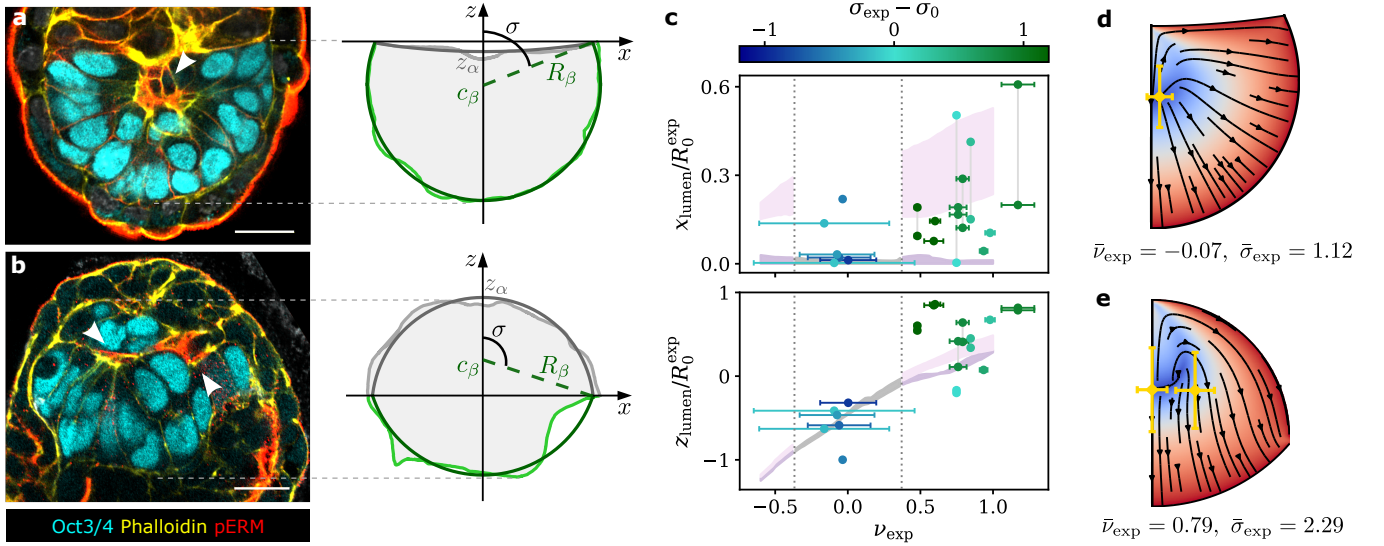


FIG. 5. **Defect positions correspond to sites of lumen nucleation in the mouse epiblast.** **a-b**, Representative immunostaining images show the central cross-section of a control (**a**) and a shape-manipulated (**b**) mouse embryo developed *ex vivo* for 18 hours from embryonic day 4.5, stained for an apical surface marker (pERM), actin, and Oct3/4. Lumen initiation sites are highlighted with white arrows. Scale bars 20 μm . To quantify the boundary shapes, we fit segmentations (light green: tissue–ECM boundary, light gray: tissue–tissue boundary) with a combination of two spherical caps, where the base is centered at $(0, c_\beta)$. This generalised acorn family is parameterised by $\sigma \equiv \cos^{-1}(-c_\beta/R_\beta)$ and $\nu \equiv z_\alpha/R_\beta$. **c**, Lumen centroid positions plotted against individually fitted ν_{exp} show that control embryos ($N = 6$) with shapes $\nu \in (-\nu_c, \nu_c)$ (dotted lines) contain single lumina, whereas 6 out of 10 embryos with shapes perturbed beyond the transition point present additional sites (vertical lines connect lumina from the same embryo). Shaded regions show the defect position ranges for ideal acorns with $\lambda/R_0 = 10^6$ and $\xi/R_0 \in [0.4, 100]$ as in Fig. 4b, and the colour code represents the difference between σ_{exp} and $\sigma_0 = \pi/2$, i.e., the deviation from the ideal acorn shape. The volume V_0^{exp} of the epiblast tissue defines $R_0^{\text{exp}} = (3V_0^{\text{exp}}/4\pi)^{1/3}$ for each embryo. Error bars are determined by residual bootstrapping of the epiblast boundaries (see [Methods](#)). **d-e**, The average initial lumen positions (yellow diamonds) are close to where the OP field for the average shape of control (**d**) and manipulated (**e**) epiblasts, characterised by $\bar{\nu}_{\text{exp}}$ and $\bar{\sigma}_{\text{exp}}$, presents defects. Error bars denote the standard deviation.

tissue made up of apico-basally polarised cells—we find that defects guide the formation of fluid-filled lumina. Even though lumina fulfill critical biological functions associated with tissue organisation and cell fate specification [64–66], it is an open question how their spatial arrangement within a tissue arises. The molecular processes that drive lumen formation in the epiblast as well as many other tissues [61], such as the active pumping of osmolytes, localize to structures at the apical side of cells [58, 59]. That defect points mark spatial regions where apical surfaces come together and lumina nucleate is therefore likely, and we indeed found that defect positions are quantitative parameter-free predictors of lumen nucleation sites in this system. Moreover, we accomplished inducing additional lumen nucleation sites by experimentally perturbing the boundary geometry beyond the transition point, where the correspondingly confined polar fluid acquires an additional defect structure. That the spatial distribution of early luminal structures follows the predicted geometry-dependent changes suggests that embryo shape regulates lumen formation via orientational effects. Lumen formation could serve as a shape-sensing checkpoint mechanism in the embryo that determines successful development of the amniotic cavity.

It will be exciting to investigate the interplay between surface-induced alignment and boundary geometry in other experimental systems to challenge the generality of this mechanism for the spatial organisation of defect-associated structures. Importantly, because the defect configurations depend almost exclusively on the geometry, the relevant observables are directly accessible from imaging data. Quantitative predictions can be made without fitting of parameters, indeed without having to make detailed assumptions about specific bulk or surface properties of the system. Aside from rendering experimental testing feasible, this robustness implies that the spatial control of defect-associated processes via boundary geometry we report likely occurs across a large range of systems with orientational degrees of freedom independent of specific material properties.

For multicellular systems in particular, our formalism provides a general and tractable framework for studying cell–ECM interactions. Traditionally considered a static environment and support structure for cells, the ECM is receiving renewed interest with recent research revealing many novel roles in determining cell behaviour (see Ref. [67] and references therein). We showed that surface alignment is a useful paradigm to describe the coupling between cellular polarity and extracellular materials such as basement membranes. Capturing the underlying physico-chemical interactions with a single effective anchoring parameter will permit investigating also the effects of feedback between geometry changes and boundary-induced order due to active ECM remodeling by cellular processes—properties distinguishing multicellular systems from passive anisotropic materials in confinement.

In conclusion, our investigations reveal how boundary geometry controls defect configurations within polar materials, and uncover a new biological function for 3D polar defects in multicellular systems. More broadly, that shape can control defect configurations independently of material specifics constitutes a general geometry-dependent organizational principle. Having demonstrated its predictive power in a system as complex and intractable as a living embryo, we expect this defect control mechanism to be relevant in diverse orientational systems.

METHODS

Geometrical definitions

Ideal acorn

If the total volume V_0 of the system is fixed, geometrical parameters c_α , R_α and R_β (see Fig. 1e in the main text) are defined solely by $\nu \equiv z_\alpha/R_\beta$ through the system of equations

$$\begin{cases} R_\alpha^2 = R_\beta^2 + c_\alpha^2 \\ \nu R_\beta = c_\alpha + \text{sgn } \nu R_\alpha \\ V_0 = \frac{2\pi}{3} R_\beta^3 + \text{sgn } \nu \frac{\pi}{3} (R_\alpha - |c_\alpha|)^2 (2R_\alpha + |c_\alpha|) \end{cases} . \quad (7)$$

The cap S_α —representing the tissue–tissue interface—can be parameterised in spherical coordinates as $r = r_\alpha(\theta) = c_\alpha \cos \theta + \sqrt{R_\alpha^2 - c_\alpha^2 \sin^2 \theta}$ for $\theta \in [0, \pi/2]$ (respectively $\theta \in [\pi/2, \pi]$) if $\nu > 0$ (respectively $\nu < 0$). Note that this includes $\nu = 1$, since in that case $c_\alpha = 0$ and $R_\alpha = R_\beta$. If $\nu = 0$, however, S_α is given by the disk with $r \in [0, R_\beta]$ and $\theta = \pi/2$. Finally, the base S_β —corresponding to the tissue–ECM interface—is simply $r = R_\beta$ and $\theta \in [\pi/2, \pi]$ for all

ν . In all cases, $\phi \in [0, 2\pi)$. With these definitions, the mixed preferred orientation in the spherical basis consists of $\mathbf{p}_0^\beta = (1, 0, 0) \forall \nu$ on S_β , and

$$\mathbf{p}_0^\alpha = \begin{cases} (1, 0, 0) & \text{if } \nu = 0 \\ (\sin \theta - \operatorname{sgn} \nu g_\alpha(\theta) \sin \theta \cos \theta, \cos \theta + \operatorname{sgn} \nu g_\alpha(\theta) \sin^2 \theta, 0) & \text{if } 0 < |\nu| < 1 \\ (0, 1, 0) & \text{if } \nu = 1 \end{cases} \quad (8)$$

with

$$g_\alpha(\theta) = \frac{r_\alpha(\theta)}{\sqrt{R_\alpha^2 - r_\alpha^2(\theta) \sin^2 \theta}} \quad (9)$$

on S_α . The tissue–tissue interaction could in principle be modelled as nematic, but since the outward-normal p_0^β imposed by the tissue–ECM boundary and the polar character of the constituents break this symmetry and favour the North-South orientation given by p_0^α we expect no significant difference.

Generalised acorn

In a more general scenario, the base S_β of the acorn can be centered at a point $(0, c_\beta)$ different from the origin of coordinates. Such a system can be characterised by two dimensionless parameters: ν , as introduced before, and $\sigma \equiv \cos^{-1}(-c_\beta/R_\beta)$ (see Figs. 5a and 5b in the main text). Considering a constant volume V_0 , the equations that geometrical parameters c_α , R_α , c_β and R_β must satisfy are

$$\begin{cases} R_\alpha^2 = R_\beta^2 + (c_\beta - c_\alpha)^2 + 2(c_\beta - c_\alpha)R_\beta \cos \sigma \\ \nu R_\beta = c_\alpha + \operatorname{sgn} \nu R_\alpha \\ V_0 = \frac{\pi}{3} R_\beta^3 (2 - \cos \sigma) (1 + \cos \sigma)^2 + \nu \frac{\pi}{6} R_\beta^3 (3 \sin^2 \sigma + \nu^2) \end{cases} \quad (10)$$

While S_α remains the same as in the ideal case, S_β is now too a spherical cap with its radius given by $r = r_\beta(\theta) = c_\beta \cos \theta + \sqrt{R_\beta^2 - c_\beta^2 \sin^2 \theta}$. By construction, however, the polar angle is still $\theta \in [\pi/2, \pi]$, and $\phi \in [0, 2\pi)$ as always. The normal to S_β is no longer a constant and is written $\mathbf{p}_0^\beta = (-\cos \theta + g_\beta(\theta) \sin^2 \theta, \sin \theta + g_\beta(\theta) \sin \theta \cos \theta, 0)$ with $g_\beta(\theta)$ defined analogously to equation (9).

Numerical details

We use the FEniCSx library DOLFINx [68] to implement the finite-element method in Python3. Given the axial symmetry of the system, the mesh (with resolution 0.05) is defined in terms of r and θ only (corresponding to a constant- ϕ slice of the 3D system). We compute the variation of \mathcal{F} [equation (2)] with respect to the 3D vector OP \mathbf{p} in the direction of a test function φ to derive its weak formulation. The resulting non-linear problem is solved using a Newton solver with a relative tolerance of 10^{-6} .

Number and type of defects in the OP field are determined by visual inspection of the phase and direction of \mathbf{p} . Utilizing that $|\mathbf{p}| \rightarrow 0$ in the vicinity of defects due to the large local distortions they induce, we infer the position of a defect as the central point of a mesh cell where $|\mathbf{p}| = 0$, surrounded by a region with $|\mathbf{p}| > 0$. The numerical uncertainty of these estimates thus depends on the size of the disordered region surrounding each defect and the resolution of the mesh. We define a threshold p^* and check in each cell whether $|\mathbf{p}| < p^*$. The value of p^* is fixed for each simulation, though we vary it conveniently from one to another in order to pre-select the least possible number of candidate points per defect (but in all cases, $p^* \leq 10^{-2}$). When more than one candidate points are selected, the location of the defect is calculated as the average of the candidate points, and error bars correspond to the standard deviation of their spatial distribution.

Culture and imaging of peri-implantation mouse embryos

To experimentally manipulate the tissue–tissue boundary in the peri-implantation mouse embryos, 3D-gel embedded embryo culture was performed as described in Ref. [37]. In brief, mouse embryos at embryonic day 4.5 were recovered from dissected uteri and cultured in a mixture of Matrigel–collagen I. Mural trophoctoderm (mTE) was microsurgically removed to enable polar trophoctoderm (pTE) invagination in the control condition, whereas maintaining mTE intact blocked pTE invagination and generated a boundary perturbation.

Embryos were fixed after 18 hours of culture with 4% paraformaldehyde (FUJIFILM Wako, 166-23251) in PBS for 30 minutes and subsequently permeabilised with 0.5% Triton X-100 (Nacalai, 12967-32) in PBS for 30 minutes. Embryos were incubated in 3% BSA (Sigma, A9647) and 0.05% Triton X-100 in PBS overnight at 4°C and then subjected to immunostaining. Primary antibodies against Oct3/4 (Santa Cruz Biotechnology, sc-5279 AF647), Collagen IV (Millipore, AB756P), and pERM (Cell Signaling, 3726) were diluted at 1:100. Donkey anti-rabbit IgG Alexa Fluor Plus 488 (Invitrogen, A32790), DAPI (Invitrogen, D3571), and Alexa Fluor Plus 555 Phalloidin (Invitrogen, A30106) were simultaneously used at the secondary antibody staining.

Images were obtained by LSM880 or LSM980 equipped with a C-Apochromat 40x/1.2 NA water immersion objective (Zeiss).

Image analysis

The epiblast tissue marked by Oct3/4 positive cells was manually segmented with Napari [69]. Labels for the entire epiblast tissue area were drawn every 30 slices with 0.16 μm interval, followed by the plugin “napari-label-interpolator” to fill the entire volume. Then the label statistics function in the plugin “napari-simpleitk-image-processing” was used to count the number of voxels of the epiblast volume. We checked that perturbation of the tissue–tissue boundary introduced only geometric changes that preserved total volume. Indeed, average epiblast tissue volume was $(1.8 \pm 0.4) \times 10^5 \mu\text{m}^3$ in the manipulated cohort and $(2.3 \pm 0.4) \times 10^5 \mu\text{m}^3$ in the control condition.

Lumen position measurement was performed based on the space encircled with pERM signals with Fiji [70], using the middle cross-section, which was extracted by the 3D rotation function in Imaris (Bitplane).

Shape model fitting

Given the collections of points $\{(x_{\mu i}^{\text{exp}}, 0, z_{\mu i}^{\text{exp}})\}_{i=1, \dots, N_\mu}$ corresponding to the segmented tissue–tissue ($\mu = \alpha$) and tissue–ECM ($\mu = \beta$) contours, we identify the centroid of the epiblast and the two points \mathbf{s}_{left} , $\mathbf{s}_{\text{right}}$ where the different boundaries meet. We define the axis of symmetry as the line passing through the centroid and perpendicular to the line between \mathbf{s}_{left} and $\mathbf{s}_{\text{right}}$; the point where these lines intersect defines the origin of coordinates. After referring the contour points to this origin, we transform them to spherical coordinates, $\{(r_{\mu i}^{\text{exp}}, \theta_{\mu i}^{\text{exp}}, 0)\}_{i=1, \dots, N_\mu} = \{\mathbf{r}_{\mu i}^{\text{exp}}\}_{i=1, \dots, N_\mu} = \mathbf{r}_\mu^{\text{exp}}$, and minimise the cost function

$$f_{\text{cost}}(\mathbf{r}_\alpha^{\text{exp}}, \mathbf{r}_\beta^{\text{exp}}; k_\alpha, c_\alpha, k_\beta, c_\beta) = \sum_{\mu=\alpha, \beta} \sum_{i=1}^{N_\mu} [\mathcal{R}(\mathbf{r}_{\mu i}^{\text{exp}}; k_\mu, c_\mu)]^2. \quad (11)$$

Here,

$$\mathcal{R}(\mathbf{r}_{\mu i}^{\text{exp}}; k_\mu, c_\mu) \equiv r_{\mu i}^{\text{exp}} - r(\theta_{\mu i}^{\text{exp}}; k_\mu, c_\mu) \quad (12)$$

is the residual between the radius of experimental point i of boundary μ and the fitting function

$$r(\theta; k_\mu, c_\mu) = c_\mu \cos \theta + \sqrt{1/k_\mu^2 - c_\mu^2 \sin^2 \theta} \quad (13)$$

evaluated at that point, with $k_\mu \equiv 1/R_\mu$ the curvature of the spherical cap and c_μ the z coordinate of its centre. To ensure continuity of the shape profile or, in other words, to guarantee a closed surface, we impose the constraint that $r(\pi/2; k_\alpha, c_\alpha) = r(\pi/2; k_\beta, c_\beta)$ at the polar angle where, by definition, the two boundaries meet. Having found the best set $\tilde{k}_\mu, \tilde{c}_\mu$, we calculate the acorn parameter

$$\nu_{\text{exp}} = \left(\tilde{c}_\alpha + \frac{\kappa}{\tilde{k}_\alpha} \right) \tilde{k}_\beta, \quad (14)$$

where $\kappa = 1$ ($\kappa = -1$) if the tissue–tissue contour is convex (concave), and the base central angle

$$\sigma_{\text{exp}} = \cos^{-1}(-\tilde{c}_\beta \tilde{k}_\beta) \quad (15)$$

that characterise the epiblast. Errors for the parameters are estimated by residual bootstrap. We generate a vector of residuals $\rho_\mu = (\delta r_{\mu 1}, \dots, \delta r_{\mu N_\mu})$, where $\delta r_{\mu i} = \mathcal{R}(\mathbf{r}_{\mu i}^{\text{exp}}; \tilde{k}_\mu, \tilde{c}_\mu)$, for each boundary μ . A residual bootstrap sample $\rho'_\mu = (\delta r'_{\mu 1}, \dots, \delta r'_{\mu N_\mu})$ is generated by randomly selecting N_μ elements from ρ_μ with replacement. Then, the cost function (11) is evaluated at the modified datasets $\mathbf{r}'_\mu^{\text{exp}} = \left\{ \left(r(\theta_{\mu i}^{\text{exp}}; \tilde{k}_\mu, \tilde{c}_\mu) + \delta r'_{\mu i}, \theta_{\mu i}^{\text{exp}}, 0 \right) \right\}_{i=1, \dots, N_\mu}$ and minimised to obtain the corresponding best set of parameters. We repeat this process for 1000 residual bootstrap samples to generate distributions of the fitting parameters, and use their standard deviation as uncertainties $\Delta \tilde{k}_\mu, \Delta \tilde{c}_\mu$. These give rise to

$$\Delta \nu_{\text{exp}} = \sqrt{\tilde{k}_\beta^2 \Delta \tilde{c}_\alpha^2 + \frac{\tilde{k}_\beta^2}{\tilde{k}_\alpha^4} \Delta \tilde{k}_\alpha^2 + \frac{\nu_{\text{exp}}^2}{\tilde{k}_\beta^2} \Delta \tilde{k}_\beta^2} \quad (16)$$

and

$$\Delta \sigma_{\text{exp}} = \sqrt{\frac{\tilde{k}_\beta^2 \Delta \tilde{c}_\beta^2 + \tilde{c}_\beta^2 \Delta \tilde{k}_\beta^2}{1 - \tilde{c}_\beta^2 \tilde{k}_\beta^2}}. \quad (17)$$

REFERENCES

- [1] N. A. Araújo, L. M. Janssen, T. Barois, G. Boffetta, I. Cohen, A. Corbetta, O. Dauchot, M. Dijkstra, W. M. Durham, A. Dussutour, *et al.*, [Soft Matter](#) **19**, 1695 (2023).
- [2] L. C. Bradley, W.-H. Chen, K. J. Stebe, and D. Lee, [Current Opinion in Colloid & Interface Science](#) **30**, 25 (2017).
- [3] A. Trushko, I. Di Meglio, A. Merzouki, C. Blanch-Mercader, S. Abuhattum, J. Guck, K. Alessandri, P. Nassoy, K. Kruse, B. Chopard, *et al.*, [Developmental cell](#) **54**, 655 (2020).
- [4] S. Harmansa, A. Erlich, C. Eloy, G. Zurlo, and T. Lecuit, [Nature Communications](#) **14**, 1220 (2023).
- [5] T. Lopez-Leon and A. Fernandez-Nieves, [Colloid and Polymer Science](#) **289**, 345 (2011).
- [6] A. Sieben, J. Schumann, and A. Seyfried, [PLoS one](#) **12**, e0177328 (2017).
- [7] J.-L. Barrat, E. Del Gado, S. U. Egelhaaf, X. Mao, M. Dijkstra, D. J. Pine, S. K. Kumar, K. Bishop, O. Gang, A. Obermeyer, *et al.*, [Journal of Physics: Materials](#) **7**, 012501 (2023).
- [8] I. Nys, [Liquid Crystals Today](#) **29**, 65 (2020).
- [9] M. Daëff, [Elveflow](#) (2020).
- [10] H. Xin, H. Chen, P. Song, and Q. Sun, [Materials Today Communications](#) , 106680 (2023).
- [11] P. Sheng, [Physical Review Letters](#) **37**, 1059 (1976).
- [12] P. Sheng, [Physical Review A](#) **26**, 1610 (1982).
- [13] G. Crawford, R. Stannarius, and J. Doane, [Physical Review A](#) **44**, 2558 (1991).
- [14] J. Nijjer, C. Li, M. Kothari, T. Henzel, Q. Zhang, J.-S. B. Tai, S. Zhou, T. Cohen, S. Zhang, and J. Yan, [Nature Physics](#) , 1 (2023).
- [15] V. Bondarenko, M. Nikolaev, D. Kromm, R. Belousov, A. Wolny, M. Blotenburg, P. Zeller, S. Rezakhani, J. Hugger, V. Uhlmann, *et al.*, [The EMBO Journal](#) , e113280 (2023).
- [16] L. E. O'Brien, T.-S. Jou, A. L. Pollack, Q. Zhang, S. H. Hansen, P. Yurchenco, and K. E. Mostov, [Nature Cell Biology](#) **3**, 831 (2001).
- [17] N. Akhtar and C. H. Streuli, [Nature Cell Biology](#) **15**, 17 (2013).
- [18] J. P. Rasmussen, S. S. Reddy, and J. R. Priess, [Development](#) **139**, 2050 (2012).
- [19] C. F. Davey and C. B. Moens, [Development](#) **144**, 187 (2017).
- [20] M. T. Butler and J. B. Wallingford, [Nature Reviews Molecular Cell biology](#) **18**, 375 (2017).
- [21] B. Ladoux, R.-M. Mège, and X. Trepast, [Trends in Cell Biology](#) **26**, 420 (2016).
- [22] K. H. Palmquist, S. F. Tiemann, F. L. Ezzeddine, S. Yang, C. R. Pfeifer, A. Erzberger, A. R. Rodrigues, and A. E. Shyer, [Cell](#) **185**, 1960 (2022).
- [23] F. N. Vicente and A. Diz-Muñoz, [Current Opinion in Systems Biology](#) , 100446 (2023).
- [24] C. E. Buckley and D. St Johnston, [Nature Reviews Molecular Cell biology](#) **23**, 559 (2022).
- [25] R. Ienaga, K. Beppu, and Y. T. Maeda, [Soft Matter](#) **19**, 5016 (2023).
- [26] F. Vafa, D. R. Nelson, and A. Doostmohammadi, [arXiv preprint arXiv:2310.06022](#) (2023).
- [27] A. Ardaševa and A. Doostmohammadi, [Nature Reviews Physics](#) **4**, 354 (2022).
- [28] K. Copenhagen, R. Alert, N. S. Wingreen, and J. W. Shaevitz, [Nature Physics](#) **17**, 211 (2021).
- [29] Y. Maroudas-Sacks, L. Garion, L. Shani-Zerbib, A. Livshits, E. Braun, and K. Keren, [Nature Physics](#) **17**, 251 (2021).
- [30] H. Li, X.-q. Shi, M. Huang, X. Chen, M. Xiao, C. Liu, H. Chaté, and H. Zhang, [Proceedings of the National Academy of Sciences](#) **116**, 777 (2019).
- [31] Y. I. Yaman, E. Demir, R. Vetter, and A. Kocabas, [Nature Communications](#) **10**, 2285 (2019).
- [32] K. Kawaguchi, R. Kageyama, and M. Sano, [Nature](#) **545**, 327 (2017).

- [33] T. B. Saw, A. Doostmohammadi, V. Nier, L. Kocgozlu, S. Thampi, Y. Toyama, P. Marcq, C. T. Lim, J. M. Yeomans, and B. Ladoux, *Nature* **544**, 212 (2017).
- [34] C. Blanch-Mercader, V. Yashunsky, S. Garcia, G. Duclos, L. Giomi, and P. Silberzan, *Physical Review Letters* **120**, 208101 (2018).
- [35] C. Blanch-Mercader, P. Guillamat, A. Roux, and K. Kruse, *Physical Review E* **103**, 012405 (2021).
- [36] C. Blanch-Mercader, P. Guillamat, A. Roux, and K. Kruse, *Physical Review Letters* **126**, 028101 (2021).
- [37] T. Ichikawa, H. T. Zhang, L. Panavaite, A. Erzberger, D. Fabrèges, R. Snajder, A. Wolny, E. Korotkevich, N. Tsuchida-Straeten, L. Hufnagel, *et al.*, *Developmental Cell* **57**, 373 (2022).
- [38] I. Bedzhov and M. Zernicka-Goetz, *Cell* **156**, 1032 (2014).
- [39] F. Jülicher, S. W. Grill, and G. Salbreux, *Reports on Progress in Physics* **81**, 076601 (2018).
- [40] P.-G. De Gennes, *Molecular Crystals and Liquid Crystals* **12**, 193 (1971).
- [41] J. V. Selinger, *Liquid Crystals Reviews* **6**, 129 (2018).
- [42] A. Rapini and M. Papoular, *Le Journal de Physique Colloques* **30**, C4 (1969).
- [43] P. Prinsen and P. Van Der Schoot, *Physical Review E* **68**, 021701 (2003).
- [44] S. R. Seyednejad, M. R. Mozaffari, and M. R. Ejtehadi, *Physical Review E* **88**, 012508 (2013).
- [45] N. J. Mottram and C. J. Newton, *arXiv preprint arXiv:1409.3542* (2014).
- [46] A. Mertelj and D. Lisjak, *Liquid Crystals Reviews* **5**, 1 (2017).
- [47] O. Prishchepa, A. Shabanov, and V. Y. Zyryanov, *Physical Review E* **72**, 031712 (2005).
- [48] M. Ravnik and S. Žumer, *Liquid Crystals* **36**, 1201 (2009).
- [49] I. I. Smalyukh, *Annual Review of Condensed Matter Physics* **9**, 207 (2018).
- [50] L. Tran, M. O. Lavrentovich, D. A. Beller, N. Li, K. J. Stebe, and R. D. Kamien, *Proceedings of the National Academy of Sciences* **113**, 7106 (2016).
- [51] A. Mietke, V. Jemseena, K. V. Kumar, I. F. Sbalzarini, and F. Jülicher, *Physical Review Letters* **123**, 188101 (2019).
- [52] M. A. Molè, A. Weberling, R. Fässler, A. Campbell, S. Fishel, and M. Zernicka-Goetz, *Cell Reports* **34** (2021), 10.1016/j.celrep.2021.108834.
- [53] G. Volovik and O. Lavrentovich, *Journal of Experimental and Theoretical Physics* **85**, 1997 (1983).
- [54] Q. Liu, B. Senyuk, M. Tasinkevych, and I. I. Smalyukh, *Proceedings of the National Academy of Sciences* **110**, 9231 (2013).
- [55] G. Duclos, R. Adkins, D. Banerjee, M. S. Peterson, M. Varghese, I. Kolvin, A. Baskaran, R. A. Pelcovits, T. R. Powers, A. Baskaran, *et al.*, *Science* **367**, 1120 (2020).
- [56] S. Mkaddem and E. Gartland Jr, *Physical Review E* **62**, 6694 (2000).
- [57] L. A. Hoffmann, L. N. Carenza, J. Eckert, and L. Giomi, *Science Advances* **8**, eabk2712 (2022).
- [58] S. M. Paul, M. Ternet, P. M. Salvaterra, and G. J. Beitel, *Development* **130**, 4963–4974 (2003).
- [59] L. Rathbun, E. Colicino, J. Manikas, J. O’Connell, N. Krishnan, N. Reilly, S. Coyne, G. Erdemci-Tandogan, A. Garrastegui, J. Freshour, *et al.*, *Nature Communications* **11**, 1269 (2020).
- [60] D. M. Bryant, A. Datta, A. E. Rodríguez-Fraticelli, J. Peränen, F. Martín-Belmonte, and K. E. Mostov, *Nature Cell Biology* **12**, 1035 (2010).
- [61] S. Sigurbjörnsdóttir, R. Mathew, and M. Leptin, *Nature Reviews Molecular Cell biology* **15**, 665 (2014).
- [62] N. Christodoulou, A. Weberling, D. Strathdee, K. I. Anderson, P. Timpson, and M. Zernicka-Goetz, *Nature Communications* **10**, 3557 (2019).
- [63] P. Guillamat, C. Blanch-Mercader, G. Pernollet, K. Kruse, and A. Roux, *Nature Materials* **21**, 588 (2022).
- [64] S. Durdu, M. Iskar, C. Revenu, N. Schieber, A. Kunze, P. Bork, Y. Schwab, and D. Gilmour, *Nature* **515**, 120 (2014).
- [65] A. Q. Ryan, C. J. Chan, F. Graner, and T. Hiiragi, *Developmental Cell* **51**, 684 (2019).

- [66] Y. S. Kim, R. Fan, L. Kremer, N. Kuempel-Rink, K. Mildner, D. Zeuschner, L. Hekking, M. Stehling, and I. Bedzhov, *Science Advances* **7**, eabe1640 (2021).
- [67] A. P. Liu, O. Chaudhuri, and S. H. Parekh, *Integrative Biology* **9**, 383 (2017).
- [68] M. W. Scroggs, J. S. Dokken, C. N. Richardson, and G. N. Wells, *ACM Transactions on Mathematical Software* **48** (2022), 10.1145/3524456.
- [69] J. Ahlers, D. Althviz Moré, O. Amsalem, A. Anderson, G. Bokota, P. Boone, J. a. Bragantini, G. Buckley, A. Burt, M. Bussonnier, *et al.*, “napari: a multi-dimensional image viewer for python,” (2023).
- [70] J. Schindelin, I. Arganda-Carreras, E. Frise, V. Kaynig, M. Longair, T. Pietzsch, S. Preibisch, C. Rueden, S. Saalfeld, B. Schmid, *et al.*, *Nature Methods* **9**, 676 (2012).

DATA AVAILABILITY

The data that support the findings of this study will be made public upon publication.

CODE AVAILABILITY

All the codes that support this study are available at <https://git.embl.de/guruciag/geometry-driven-defects>.

ACKNOWLEDGEMENTS

We thank R. Belousov, V. Bondarenko, T. Dullweber, J. Ellenberg, J. Elliott, I. Estabrook, L. Manning, T. Quail, J. Rombouts, and A. Torres Sánchez for useful discussions and valuable feedback on the manuscript. The Erzberger group is funded by the EMBL. The Hiiragi laboratory was supported by the EMBL, and currently by the Hubrecht Institute, the European Research Council (ERC Advanced Grant “SelforganisingEmbryo” grant agreement 742732, ERC Advanced Grant “COORDINATION” grant agreement 101055287), Stichting LSH-TKI (LSHM21020), and Japan Society for the Promotion of Science (JSPS) KAKENHI grant numbers JP21H05038 and JP22H05166. P.C.G. is supported by Marie Skłodowska-Curie Actions COFUND through an EMBL Interdisciplinary Postdoctoral Fellowship (EIPOD4, grant agreement 847543), and an Add-on Fellowship for Interdisciplinary Life Science of the Joachim Herz Stiftung. P.C.G. thanks Kyoto University for its hospitality during part of the preparation of this work.

AUTHOR CONTRIBUTIONS

All authors designed the research. P.C.G. performed the numerical simulations. T.I. performed the experiments. T.I. and P.C.G. analysed the data and fitted the shape model. P.C.G. prepared the figures with input from A.E. P.C.G. and A.E. wrote the paper with contributions from T.I. and T.H.

COMPETING INTERESTS

The authors declare no competing interests.

SUPPLEMENTARY INFORMATION

Derivation of the Euler-Lagrange equations

In order to find the value of the vector field $\mathbf{p}(\mathbf{r})$ that minimises the free energy functional

$$\mathcal{F}[\mathbf{p}] = \int_{\Omega} dV f_{\text{B}}(\mathbf{p}, \nabla \mathbf{p}) + \int_{\partial\Omega} dS f_{\text{S}}(\mathbf{p}), \quad (1)$$

in a volume Ω , we write the variation

$$\delta\mathcal{F} = \int_{\Omega} dV \left[\frac{\partial f_{\text{B}}}{\partial p_i} \delta p_i + \frac{\partial f_{\text{B}}}{\partial (\nabla p_i)} \cdot \nabla (\delta p_i) \right] + \int_{\partial\Omega} dS \frac{\partial f_{\text{S}}}{\partial p_i} \delta p_i, \quad (2)$$

where Einstein summation convention over repeated indexes is used. The second term of the volume integral can be integrated by parts to yield

$$\begin{aligned} \int_{\Omega} dV \frac{\partial f_{\text{B}}}{\partial (\nabla p_i)} \cdot \nabla (\delta p_i) &= \int_{\Omega} dV \left\{ -\nabla \cdot \left[\frac{\partial f_{\text{B}}}{\partial (\nabla p_i)} \right] \delta p_i + \nabla \cdot \left[\frac{\partial f_{\text{B}}}{\partial (\nabla p_i)} \delta p_i \right] \right\} \\ &= - \int_{\Omega} dV \nabla \cdot \left[\frac{\partial f_{\text{B}}}{\partial (\nabla p_i)} \right] \delta p_i + \int_{\partial\Omega} dS \hat{\mathbf{n}} \cdot \frac{\partial f_{\text{B}}}{\partial (\nabla p_i)} \delta p_i \end{aligned} \quad (3)$$

with $\hat{\mathbf{n}}$ the outward normal. Thus, equation (2) becomes

$$\delta\mathcal{F} = \int_{\Omega} dV \left[\frac{\partial f_{\text{B}}}{\partial p_i} - \nabla \cdot \frac{\partial f_{\text{B}}}{\partial (\nabla p_i)} \right] \delta p_i + \int_{\partial\Omega} dS \left[\frac{\partial f_{\text{S}}}{\partial p_i} + \hat{\mathbf{n}} \cdot \frac{\partial f_{\text{B}}}{\partial (\nabla p_i)} \right] \delta p_i. \quad (4)$$

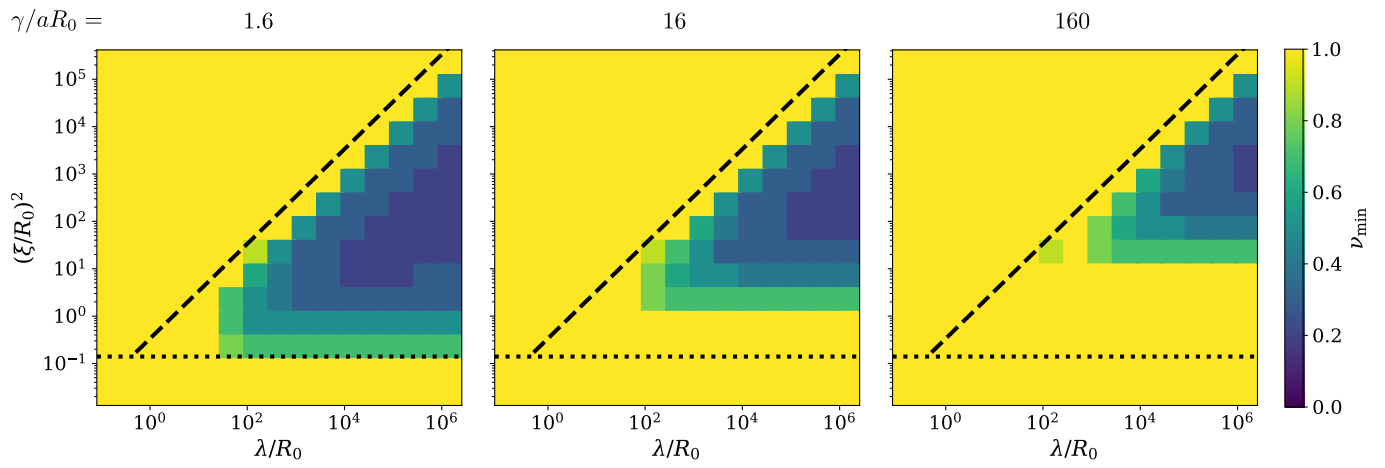
If the minimising field \mathbf{p} were to have a fixed value on the boundary (essential boundary conditions), $\delta p_i|_{\partial\Omega} = 0$ and the surface integral would vanish directly. In our case, however, we take boundary conditions on \mathbf{p} to be natural, meaning that they are not imposed externally, but are *naturally* derived from the problem and satisfied after a solution has been found. Hence, for arbitrary variations δp_i , we enforce

$$\frac{\partial f_{\text{S}}}{\partial p_i} + \hat{\mathbf{n}} \cdot \frac{\partial f_{\text{B}}}{\partial (\nabla p_i)} = 0 \quad \text{in } \partial\Omega. \quad (5)$$

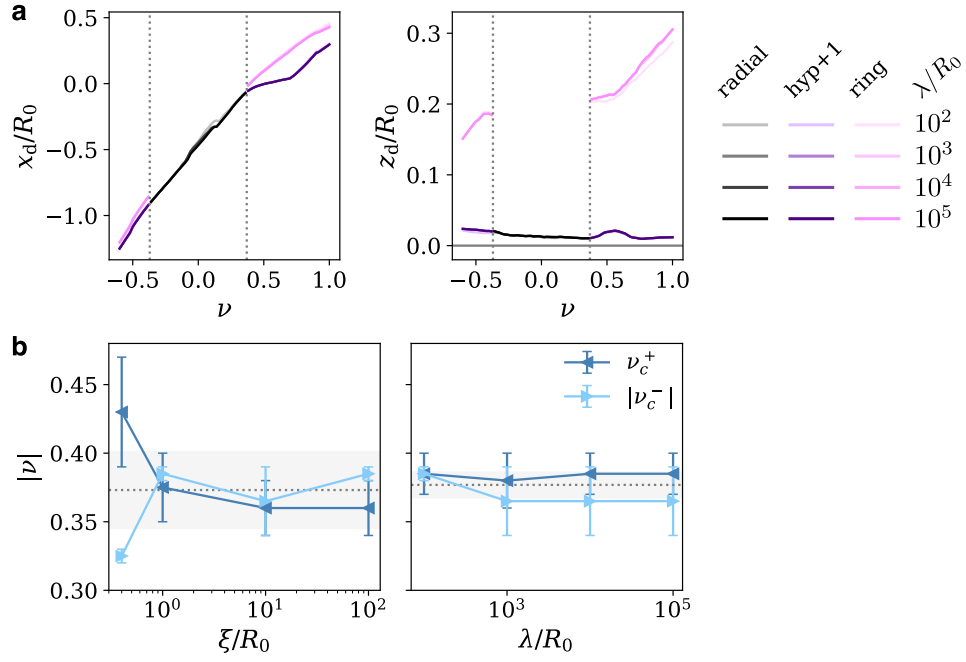
These equations ensure continuity of \mathbf{p} on the surface and leave us only with the volume integral. Finally, asking that $\delta\mathcal{F} = 0$ gives rise to the set of coupled partial differential equations

$$\frac{\partial f_{\text{B}}}{\partial p_i} - \nabla \cdot \frac{\partial f_{\text{B}}}{\partial (\nabla p_i)} = 0 \quad \text{in } \Omega, \quad (6)$$

which are the Euler-Lagrange equations of the problem.



Extended Data Fig. 1. **Surface tension favours the spherical shape.** Since the surface tension favours shapes with smaller surface-to-volume ratios, the transition between spherical and non-spherical systems at small correlation lengths moves to greater values on increasing γ .



Extended Data Fig. 2. **The position of defects and the transitions between them are robust to parameter changes.**

a, Within the highly ordered regime, the location of the defects is not affected by a three order of magnitude variation of the anchoring length. Here, $\xi/R_0 = 1$. **b**, The critical value of the acorn parameter where the transition between defect configurations occurs, $\nu_c = 0.37 \pm 0.03$ (dotted lines and shaded area), is independent on the mechanical parameters. It is also not affected by the sign of the cap curvature, with ν_c being approximately the same in absolute value for convex and concave caps.